Canadian Geotechnical Journal (Author Accepted Manuscript)
Version of Record at: https://doi.org/10.1139/cgj-2022-0246

For personal use only. This Just-IN manuscript is the accepted manuscript prior to copy editing and page composition. It may differ from the final official version of record.

Three-dimensional stress-strain and strength behavior of silt-clay transition soils

Pongpipat Anantanasakul[1,*]; Phimmawat Intharachart[2]; Victor N. Kaliakin[3]

[1]Assistant Professor, Department of Civil and Environmental Engineering, Mahidol University, Nakhon Pathom 73170, Thailand (Corresponding Author, E-mail: pongpipat.ana@mahidol.ac.th)

[2]Graduate Assistant, Department of Civil and Environmental Engineering, Mahidol University, Nakhon Pathom 73170, Thailand

[3]Professor, Department of Civil and Environmental Engineering, University of Delaware, Newark, DE 19716, USA

© The Author(s) or their Institution(s)

Version of Record at: https://doi.org/10.1139/cgj-2022-0246

For personal use only. This Just-IN manuscript is the accepted manuscript prior to copy editing and page composition. It may differ from the final official version of record.

Abstract

The effect of silt content on the mechanical behavior of silt-clay transition soils under three-dimensional stress conditions is presented. Undrained true triaxial tests with constant b values were performed on normally consolidated specimens of silt-clay transition soils created from the same base clay and non-plastic silt, however, with systematically varying gradations. With increasing amount of non-plastic silt, the cohesive soils exhibit less contractive tendencies, stiffer stress-strain response and larger shear strength. The magnitude of intermediate principal stress, as indicated by the b value, also strongly influences the stress-strain relations, pore pressure behavior and both total and effective failure surfaces. Although the transition soils exhibit overall clay-like behavior, more pronounced frictional characteristics, as indicated by the shapes of the failure and plastic potential surfaces, were exhibited with increasing silt content.

Key words: Silt-clay soil; Stress-strain; Shear strength; Silt content; True triaxial test.

© The Author(s) or their Institution(s)

Canadian Geotechnical Journal (Author Accepted Manuscript)
Version of Record at: https://doi.org/10.1139/cgj-2022-0246

For personal use only. This Just-IN manuscript is the accepted manuscript prior to copy editing and page composition. It may differ from the final official version of record.

Introduction

Large deposits of fine-grained cohesive soils are present in several metropolitan areas around the world. These urban areas, which include Bangkok, San Francisco, London and Shanghai among others, are densely populated and experience a rather large amount of geotechnical activities such as tunneling, deep excavation and construction of deep foundations and shoreline structures. The cohesive soils found in the aforementioned deposits are often of the same geological origin and consist of particles with identical basic minerals. However, the soil formation process, which is usually affected by environmental factors such as a marine transgression-regression sequence, often results in soil particle-size distributions that vary from one location to another. Such variation in particle gradation, and thus mineral content, results in different plasticity characteristics, as indicated by the consistency or Atterberg limits. This, in turn, creates an array of cohesive soils that, in terms of both engineering classification and fundamental behavior, transition from one general soil type to another even within essentially similar deposits. The mechanical behavior of such "transition" soils can thus vary rather significantly.

The stress-strain and strength characteristics of cohesive soils have been rather extensively investigated by means of laboratory tests. Very often, the stress conditions pertaining to such tests are axisymmetric, with the major principal stress (σ_1) in the axial direction being greater than the intermediate and minor principal stresses, which are equal in the radial directions (i.e., $\sigma_2 = \sigma_3$). Geostructures such as diaphragm walls, piled raft foundations, shafts and tunnels, however, rarely result in axisymmetric triaxial stress conditions in the soil mass; instead, the stress conditions tend to be plane-strain or three-dimensional, where $\sigma_1 > \sigma_2 > \sigma_3$. Laboratory tests that permit application of unequal principal stresses during shear are thus essential to better understanding the overall mechanical response of cohesive soils. Based on the aforementioned rationale, it is thus imperative for geotechnical engineers to gain insight into

© The Author(s) or their Institution(s)

Version of Record at: https://doi.org/10.1139/cgj-2022-0246
For personal use only. This Just-IN manuscript is the accepted manuscript prior to copy editing and page composition. It may differ from the final official version of record.

the stress-strain and strength behavior of "transition" cohesive soils that are subjected to realistic three-dimensional stress states. Such insight impacts geotechnical considerations and allows for more effective analysis and design of geostructures constructed in or with such soils.

Previous studies

The stress-strain and strength behavior of cohesive soils with varying silt and clay contents has been studied by a rather small number of researchers (e.g., Yin 1999; Cola and Simonini 2002; Yin 2002, Nocilla et al. 2006; Anantanasakul et al. 2012a; Wang and Luna 2012; Wong et al. 2017; Anantanasakul and Roth 2018). Fine-grained soils with low silt-sized particle contents ($0.075 \geq D \geq 0.002$ mm), high clay-sized particle contents ($D < 0.002$ mm) and sufficiently high values of plasticity index (PI) have been observed to fundamentally exhibit clay-like or cohesive behavior. Here D is the diameter of a hypothetical spherical soil particle. With higher silt contents and lower clay contents, such cohesive soils exhibit lower plasticity, as determined by the PI, and become less compressible when consolidated one-dimensionally or isotropically. As the silt content increases, the results of triaxial tests show stiffer stress-strain response, larger undrained shear strength and higher effective friction angles. During axisymmetric triaxial compression tests, volume changes and pore pressure changes generally decrease, thus indicating more dilative tendencies with increasing silt content and decreasing clay content. For increasing degrees of overconsolidation, increased normalized undrained shear strengths have been observed for cohesive soils with higher silt contents.

At sufficiently high silt contents and low clay contents, fine-grained soils with low PI values start to fundamentally exhibit sand-like or cohesionless behavior. They exhibit much lower compressibility when consolidated, more pronounced dilative response during shear and, apparently, no unique relationship between void ratio and effective mean stress at critical state or failure (Ferreira and Bica 2006).

© The Author(s) or their Institution(s)

Canadian Geotechnical Journal (Author Accepted Manuscript)
Version of Record at: https://doi.org/10.1139/cgj-2022-0246

For personal use only. This Just-IN manuscript is the accepted manuscript prior to copy editing and page composition. It may differ from the final official version of record.

In an attempt to quantify the aforementioned response, Boulanger and Idriss (2006) proposed a practical criterion to delineate fine-grained soils exhibiting clay-like behavior. According to this criterion, fine-grained soils behave as a clay when PI $\geq$ 7; for the narrow range of 7 > PI $\geq$ 3, a transition from clay-like to sand-like behavior is usually observed; finally, for PI < 3, fine-grained soils exhibit essentially sand-like response.

More insight into the three-dimensional behavior of cohesive soils can be obtained by means of soil testing apparatuses that permit application of unequal principal stresses with or without rotation of the principal stress directions. For tests that do not involve the rotation of principal stresses, only normal stresses are applied to the orthogonal faces of either cubical or prismatic specimens (e.g., Yin et al. 2010; Anantanasakul et al. 2012b). Past research has indicated significant influence of the relative magnitude of the intermediate principal stress on the stress-strain, volume change, pore pressure change and strength characteristics of cohesive soils (e.g., Matsuoka et al. 2002). In general, the relative magnitude of the intermediate principal stress may conveniently be expressed by means of the b value:

$$b = \frac{\sigma_2 - \sigma_3}{\sigma_1 - \sigma_3} \quad [1]$$

where $0 \leq b \leq 1$. For axisymmetric triaxial compression with $\sigma_2 = \sigma_3$, b is equal to zero; for axisymmetric triaxial extension in which $\sigma_2 = \sigma_1$, b is equal to unity.

A rather small number of studies have investigated the effects of b value on the behavior of clays using true triaxial apparatuses that allow independent control of all three principal stresses (Nakai et al. 1986; Kirkgard and Lade 1993; Prashant and Penumadu 2005; Anantanasakul et al. 2012b). It has been reported that values of elastic modulus increase, principal strains-to-failure in the direction of major principal stress decrease and pore pressure changes at failure, in general, increase with increasing b values. Effective friction angles increase from their value for b = 0.0, remain relatively constant throughout a range of increasing intermediate b values,

© The Author(s) or their Institution(s)

Version of Record at: https://doi.org/10.1139/cgj-2022-0246

For personal use only. This Just-IN manuscript is the accepted manuscript prior to copy editing and page composition. It may differ from the final official version of record.

and decrease slightly as b approaches unity. The results of true triaxial tests also indicate that failure surfaces in the octahedral plane are curved and circumscribe the Mohr-Coulomb failure surfaces when fitted to the friction angles in triaxial compression (i.e., for $b = 0.0$).

Missing from past true triaxial testing programs is a systematic investigation into the effects that variations in b value and silt content have on the behavior of silt-clay "transition" soils. The experimental study described in this paper was thus undertaken to fill this void in information.

Presented herein are the results of a laboratory study of the influence of the relative magnitude of intermediate principal stress and silt content on the stress-strain, pore pressure change and strength characteristics of silt-clay transition soils. Undrained true triaxial tests with different constant b values were performed on normally consolidated specimens of such soils. Conventional undrained triaxial tests with varying effective consolidation pressures were also performed to investigate the behavior of silt-clay transition soils under axisymmetric stress conditions. In this study the same base clay and silt, specimen preparation procedure, testing methods, and testing conditions were used. Only the amount of silt in the specimens was systematically varied.

Soils tested

The two base soils employed in this study were kaolin clay and silt. The inorganic clay was obtained from a uniform natural deposit in Lampang, Thailand. It was supplied as bulk samples with delivery water contents of 7-10%. These samples were oven dried and ground to produce fine clay powder. The silt consisted of ground silica, sieved to obtain a specific particle-size gradation. It was essentially non-plastic.

Three laboratory-prepared soils were used to study the stress-strain, pore pressure change and strength behavior of silt-clay transition soils. In the subsequent development, the pure

© The Author(s) or their Institution(s)

Canadian Geotechnical Journal (Author Accepted Manuscript)
Version of Record at: https://doi.org/10.1139/cgj-2022-0246

For personal use only. This Just-IN manuscript is the accepted manuscript prior to copy editing and page composition. It may differ from the final official version of record.

kaolin clay will be referred to as "Soil 1". The other two soils were created by mixing Soil 1 with different amounts of non-plastic silt. These two silt-clay mixtures will be referred to as Soils 2 and 3, respectively. Fig. 1 shows the particle-size gradations for Soils 1, 2 and 3, as determined from wet sieve and hydrometer analyses (ASTM D422-63). The grain-size distribution curve for the non-plastic silt is also plotted in Fig. 1 for comparison. This curve indicates that the silt consisted only of silt-sized particles and was fairly well graded.

Table 1 lists the clay, silt and sand contents of the three soils. Also given in this table are values of the liquid limit, plasticity index and Skempton's activity coefficient for each of these soils. The liquid limits and plasticity indices decrease with increases in the amount of non-plastic silt. As the amount of non-plastic silt increases from 0 to 71%, the values of activity coefficient decrease from 0.27 to 0.20. According to the Unified Soil Classification System (USCS), Soils 1, 2 and 3 classify as MH (i.e., silt with high plasticity), ML and ML (silt with low plasticity), respectively.

Preparation of test specimens

Proper amounts of dry kaolin powder and non-plastic silt were mixed with water to produce slurries at water contents equal to twice the liquid limit of each of the three soils. The mixing of slurries was carried out in a commercial-grade stand mixer. The slurries were later one-dimensionally consolidated at an effective vertical stress of 150 kPa in a double-draining consolidation tank as described by Anantanasakul and Roth (2018).

Following consolidation, cake samples, 254 mm in diameter and 170 mm high, were obtained from the tank. Table 1 reports representative values of water content, void ratio and unit weight of the cake samples of the three silt-clay soils. The samples were then cut into prismatic sections. Each such section was stored in a sealed plastic bag that was kept in a humidity controlled room. The soil sections were later trimmed parallel to the direction of

Version of Record at: https://doi.org/10.1139/cgj-2022-0246

For personal use only. This Just-IN manuscript is the accepted manuscript prior to copy editing and page composition. It may differ from the final official version of record.

slurry consolidation using a wire saw to produce specimens. For the true triaxial tests, the specimens were prismatic with side lengths of 71 mm and a height of 142 mm. For the axisymmetric triaxial tests, the specimens were cylindrical with a diameter of 71 mm and a height of 142 mm.

Fig. 2 shows scanning electron micrographs of Soils 1, 2 and 3 and the non-plastic silt, magnified 1000 times. For Soils 1, 2 and 3, the micrographs were taken on consolidated samples, while that of the non-plastic silt was obtained from silt powder. The white boundaries drawn in the micrographs of Soils 2 and 3 indicate traces of large silt particles in the respective soil matrices. The micrographs illustrate an apparent transition from a homogeneous matrix of uniformly distributed clay particles and particle clusters (Soil 1) to one with an increasingly complex arrangement of clay particle clusters surrounding large silt grains. This is especially true for Soil 3. The micrograph of the non-plastic silt indicates that the soil consisted of highly angular particles of various sizes. This finding is consistent with the aforementioned well-graded grain-size distribution for non-plastic silt shown in Fig. 1.

True triaxial apparatus

Undrained shear tests with unequal principal stresses were performed on prismatic specimens of the silt-clay transition soils using the custom-made true triaxial apparatus shown in Fig. 3. The apparatus accommodates both cubical and tall prismatic specimens (height-to-width ratios of 1 to 2.7) and allows tests to be performed in a fully automated manner. It consists of an oversized triaxial cell that is fitted with a rounded square cap and base. Vertical deviator loads are applied to the specimen through a piston rod.

Deviator loads in one horizontal direction were applied by a self-reacting load frame consisting of two loading plates that are compressible in the vertical direction. One loading plate was attached to the rectangular face of an internal pressure cylinder, while the other was attached to a backing plate. The internal pressure cylinder and backing plate were attached to

Version of Record at: https://doi.org/10.1139/cgj-2022-0246

For personal use only. This Just-IN manuscript is the accepted manuscript prior to copy editing and page composition. It may differ from the final official version of record.

one another by two tie bars. One loading plate was pushed, while the opposing plate was pulled inward when the pressure cylinder was inflated. Each loading plate was made of alternating stainless steel and balsa wood laminae. The compressibility of the balsa wood permits vertical deformation of the loading plates, which is necessary to avoid interference with the cap. The A-shaped compression frame attached to the piston rod forced the loading plates to deform at the same rate of vertical deformation as the specimen.

The true triaxial apparatus applied three independent principal stresses to the specimens with no rotation of the principal stress directions. The major principal stress (σ_1) was applied in the vertical direction; the intermediate principal stress (σ_2) in the direction of the horizontal loading system; and the minor principal stress (σ_3) in the other horizontal direction.

Vertical deviator loads were measured by a submersible load cell embedded in the specimen cap. Horizontal deviator loads and cell and pore pressures were determined from pressure transducer readings. Volume changes were monitored using a volume change device similar to that described by Lade (1988). Vertical deformations of the specimen were measured by a Linear Variable Differential Transducer (LVDT). In the σ_2 direction, horizontal deformations were tracked by two submersible LVDTs. Deformations of the specimen in the σ_3 direction were computed from volume changes and from deformations in the σ_1 and σ_2 directions.

A National Instrument LabVIEW computer program was used in conjunction with the apparatus to perform true triaxial tests in an automated manner. The computer control program was based on a closed-loop PID control algorithm (Anantanasakul et al. 2012b). It continuously receives input signals from the transducers and computes the current stresses and strains on the specimen. To follow the desired stress path, target stresses and strains were assigned to the program's PID controller. This controller attempts to minimize the differences or errors between the measured stresses and strains and the targets by outputting corrective reactions to the apparatus. The reactions were converted into voltage signals, which were sent to the

© The Author(s) or their Institution(s)

Version of Record at: https://doi.org/10.1139/cgj-2022-0246

For personal use only. This Just-IN manuscript is the accepted manuscript prior to copy editing and page composition. It may differ from the final official version of record.

corresponding automatic pressure regulators, thus applying corrective loads through: 1) a diaphragm air cylinder and the cell piston in the σ_1 direction, 2) the pressure cylinder of the horizontal loading system in the σ_2 direction, and 3) the triaxial cell in the σ_3 direction. As such, the stresses and strains were readjusted and a real-time feedback control operation was formed.

Specimen installation

During the installation of a specimen into the true triaxial device, filter paper slots, cut in a vertical pattern, were attached to the specimen faces in the minor principal stress direction (Fig. 6). Parts of the slots covered filter stones located on the sides of the cap and base, thus allowing drainage from the specimen to the volume change device. Double layers of greased latex membrane, 0.3 mm thick, were applied to the cap, base and to both horizontal loading plates so as to reduce friction between the specimen and the rigid boundaries in the σ_1 and σ_2 directions. The filter paper slots and drain lines were saturated using the standard carbon dioxide (CO_2) method as detailed by Lade (2016). A constant back pressure of 100 kPa was applied to the specimens through the volume change device. The values of pore pressure coefficient B (Skempton 1954) measured after the application of back pressure in all tests were no less than 0.98, thus indicating that satisfactory degrees of saturation were attained.

Consolidated-undrained true triaxial tests

To determine the appropriate strain rate to use in performing the undrained true triaxial tests, the recommendations of Bishop and Henkel (1957) were followed. The volume change-time curves of prismatic rectangular specimens during isotropic consolidation were examined. Critical drainage conditions, in terms of time required to reach primary consolidation, were encountered in Soil 1. The coefficient of consolidation of the soil was sought, and an axial strain rate of 0.0035% per minute was determined based on the value of this coefficient. To

© The Author(s) or their Institution(s)

Canadian Geotechnical Journal (Author Accepted Manuscript)
Version of Record at: https://doi.org/10.1139/cgj-2022-0246
For personal use only. This Just-IN manuscript is the accepted manuscript prior to copy editing and page composition. It may differ from the final official version of record.

eliminate the effect of rate of shearing on the observed mechanical behavior, this strain rate was also used in all of the true triaxial tests performed on Soils 2 and 3.

Eight true triaxial tests, with constant b values of 0.0, 0.1, 0.2, 0.4, 0.6, 0.8, 0.9 and 1.0, were performed for each of the three silt-clay transition soils. In each such test, the specimen was consolidated at an isotropic effective stress of 200 kPa. Prior to shearing, all specimens were thus normally consolidated. Upon completion of primary consolidation, each specimen was sheared under undrained conditions and with a constant strain rate in the σ_1 direction. The total confining stress (σ_3) was kept constant at 300 kPa. The major principal stress (σ_1) was determined and the pressure inside the internal horizontal cylinder (and thus the intermediate principal stress σ_2) was automatically adjusted so that the desired b value during the course of shearing was maintained constant.

In addition to the aforementioned true triaxial tests, three consolidated-undrained axisymmetric triaxial compression tests at effective consolidation stresses of 200, 400 and 500 kPa were performed on cylindrical specimens of Soils 1, 2 and 3 to investigate the effect of specimen shape and consolidation pressure on the observed mechanical response. The specimen installation and testing procedures of these conventional triaxial tests have been discussed in detail by Anantanasakul and Roth (2018).

For a given value of b, the results of the undrained true triaxial tests are represented by the following three figures. First, the difference between the major and minor principal stresses ($\sigma_1 - \sigma_3$), normalized by the effective consolidation pressure (σ'_c), is plotted versus the normal strain in the σ_1 direction (ε_1). Next, the ratio of major to minor principal effective stresses (i.e., σ'_1/σ'_3) is plotted versus ε_1. Finally, the excess pore pressure (Δu), normalized by σ'_c, is plotted versus ε_1. Fig. 4 presents these three figures for each of the values of b = 0.0, 0.1, 0.2, and 0.4. Fig. 5 presents similar figures for b = 0.6, 0.8, 0.9, and 1.0. In Figs. 4 and 5, failure points, defined by states of maximum σ'_1/σ'_3, are denoted by arrows.

© The Author(s) or their Institution(s)

Version of Record at: https://doi.org/10.1139/cgj-2022-0246

For personal use only. This Just-IN manuscript is the accepted manuscript prior to copy editing and page composition. It may differ from the final official version of record.

Stress-strain response

The stress difference and effective stress ratio curves of each tested soil follow rather similar patterns. Regardless of the b value, they increase more sharply and reach higher peak values with increasing silt content. This indicates larger stiffness and higher shear resistance of the silt-clay transition soils. This is possibly due to interparticle friction among the silt grains, more of which are in contact with one another at higher silt contents. In general, the strains to failure (ε_{1f}) of the soils decreased with increased silt content. When comparing the results for Soils 1 and 3, differences in ε_{1f} by as much as 6% are observed.

For comparison, the results of undrained axisymmetric triaxial compression tests with different values of σ'_c are also plotted in the figures associated with the true triaxial test results for b = 0.0 (Fig. 4). In all cases, the axisymmetric triaxial test results are very similar to the true triaxial test results. This suggests that the specimen shapes used (i.e., prismatic in the true triaxial tests versus cylindrical in the axisymmetric tests), as well as the different values of σ'_c have a negligible effect on the normalized stress-strain response of the silt-clay soils tested.

The magnitude of intermediate principal stress, as measured by the b value, significantly influences the observed stress-strain relations. Both normalized stress difference and effective stress ratio curves gradually rise to reach peak values at relatively large values (12-15%) of ε_1 and either remain constant or slightly decrease thereafter for b values of 0.0 to 0.2. In these tests, the specimens of all tested soils underwent uniform deformations and strains up to failure. Distinct failure planes or shear bands were observed in the softening regime corresponding to the post-peak portions of the stress-strain relations in some tests. When a shear band forms and propagates, the material deformations localize into a thin zone of intense shearing. The soil specimen is separated into two rigid blocks that slide on one another along the shear band, and the stresses and strains are no longer uniform. As shown in Fig. 6, the shear bands observed in

© The Author(s) or their Institution(s)

Version of Record at: https://doi.org/10.1139/cgj-2022-0246
For personal use only. This Just-IN manuscript is the accepted manuscript prior to copy editing and page composition. It may differ from the final official version of record.

the present true triaxial tests were inclined to the σ_1 and σ_3 directions, approximately parallel to the σ_2 direction. Their offsets were always visible in the σ_3 sides of the prismatic specimens.

For higher b values, the stress-strain curves appear to be more abrupt or "brittle". They increase sharply to reach peaks or failure at relatively small values of ε_1. In some of these tests, the peaks are followed by significant reductions in strength. Shear bands were present in essentially all true triaxial tests with b-values greater than 0.2. They started to form even as the specimens were still in the hardening regime. Significant reductions in strength always accompanied shear bands that developed freely with no interference with the rigid boundaries at the top and bottom caps. For tests in which the propagating shear bands intercepted the rigid boundaries, the post-failure stress-strain curves remained relatively constant or descended only slightly.

Shear banding as a possible mode of soil failure has been studied by some researchers within the context of bifurcation analysis (e.g., Rudnicki and Rice 1975; Vermeer 1982; Vadoulakis 1996; Wang and Lade 2001; Lade 2003; Lade et al. 2008). In this framework, a criterion for shear band formation that satisfies equilibrium, compatibility, boundary conditions and constitutive relations is provided based on the magnitude of the critical plastic modulus of the soil. It has been proposed that shear bands in granular soils will form during the hardening regime of the stress-strain response for intermediate b values of about 0.2 to 0.9. For b values outside this range, shear bands will initiate in either the softening regime or when the stress-strain curve essentially attains the smooth peak point. The behavior observed in the present true triaxial tests on transition silt-clay soils appears to follow the same trend.

Shear bands form along the plane of maximum shear stresses whose orientation varies with the magnitude of major principal stress (σ_1), minor principal stress (σ_3) and the soil failure characteristics. For the prismatic specimen used in true triaxial testing (without rotation of the principal stress directions), the shear band or failure plane is inclined to the σ_1 and σ_3

© The Author(s) or their Institution(s)

Version of Record at: https://doi.org/10.1139/cgj-2022-0246

directions. Note that the soil specimen undergoes normal compressive strains in the σ_1 direction and expansive strains in the σ_3 direction. When shear banding is the mode of failure, the ease of shear band formation has been observed to relate to the rate at which ε_3 changes with respect to ε_1; i.e., $-d\varepsilon_3/d\varepsilon_1$. With increasing b value, greater confinement is provided to the specimen in the σ_2 direction (i.e., more compressive states of ε_2); the specimen is, therefore, forced to expand more in the σ_3 direction. As the result, the magnitude of ε_3 increases more sharply, thus promoting initiation and propagation of the shear band in the soil specimen.

Pore pressure response

The relationships between normalized excess pore pressure ($\Delta u/\sigma'_c$) and major principal strain are shown in Figs. 4 and 5. In general, the normalized pore pressure changes are all positive, indicating contractive tendency of the normally consolidated soils during shear under the three-dimensional stress conditions. For all three of the soils tested, the pore pressure changes sharply increase for ε_1 values less than approximately 3%. The curves then rise only marginally to reach maximum values that remain relatively constant to large strains. For all b values considered in the present study, the $\Delta u/\sigma'_c - \varepsilon_1$ curves rise more sharply and reach higher peak values with increasing silt content.

The $\Delta u/\sigma'_c - \varepsilon_1$ curves for the undrained axisymmetric triaxial compression tests are also plotted in Fig. 4. These are seen to be in good agreement with those corresponding to the true triaxial tests with b = 0.0.

The effects that variations in the principal stresses have on the magnitude of pore pressure change during shear can be further investigated by means of the pore pressure parameter $\bar{a}$ that was introduced by Henkel and Wade (1966). This parameter is applicable to saturated soils undergoing undrained shear under non-axisymmetric stress conditions. It is present in the

For personal use only. This Just-IN manuscript is the accepted manuscript prior to copy editing and page composition. It may differ from the final official version of record.

© The Author(s) or their Institution(s)

Canadian Geotechnical Journal (Author Accepted Manuscript)
Version of Record at: https://doi.org/10.1139/cgj-2022-0246

For personal use only. This Just-IN manuscript is the accepted manuscript prior to copy editing and page composition. It may differ from the final official version of record.

mathematical formulation relating a change in pore pressure to the corresponding changes in the three principal stresses; i.e.,

$$[2] \qquad \Delta u = \frac{\Delta\sigma_1 + \Delta\sigma_2 + \Delta\sigma_3}{3} + \bar{a}\sqrt{(\Delta\sigma_1 - \Delta\sigma_2)^2 + (\Delta\sigma_2 - \Delta\sigma_3)^2 + (\Delta\sigma_1 - \Delta\sigma_3)^2}$$

Positive values of $\bar{a}$ indicates a contractive tendency, while negative values represent dilative response. For the case of a conventional axisymmetric triaxial compression test, $\sigma_2 = \sigma_3$ and $\Delta\sigma_2 = \Delta\sigma_3 = 0$. In this case $\bar{a} = 3(\bar{A} - 1/3)/\sqrt{2}$, where $\bar{A} = \Delta u/\Delta\sigma_1$ is Skempton's pore pressure parameter (Skempton 1954).

The value of the Henkel and Wade pore pressure parameter corresponding to the maximum principal stress difference (i.e., $(\sigma_1 - \sigma_3)_{max}$) is denoted by $\bar{a}_f$. The variation of $\bar{a}_f$ with the value of b for each of the three soils tested as part of the present study is shown in Fig. 7. In all cases, the values of $\bar{a}_f$ are positive. For Soil 1, the $\bar{a}_f$ values continuously decrease with increasing b values, thus suggesting less contractive tendencies. For Soils 2 and 3, in the range from b = 0.0 to 0.6, the values of $\bar{a}_f$ also decrease. However, beginning at b = 0.6, the $\bar{a}_f$ values remain essentially constant. Finally, for a given value of b, the value of $\bar{a}_f$ decreases with increasing amount of non-plastic silt.

At the critical state, the principal stress differences and excess pore pressures cease to change, even though the shear strain continues to increase. Based on the results shown in Figs. 4 and 5, it appears that for the three normally consolidated silt-clay soils tested, critical state is approached for values of b = 0.0 to 0.2. For larger b values, shear bands developed in the specimens, causing significant reductions in $(\sigma_1 - \sigma_3)/\sigma'_c$ with increasing strain. Thus, unlike the $\Delta u/\sigma'_c - \varepsilon_1$ response which remained essentially constant at larger values of strain, the principal stress differences do not, strictly speaking, attain critical states for $b > 0.2$.

© The Author(s) or their Institution(s)

Version of Record at: https://doi.org/10.1139/cgj-2022-0246

For personal use only. This Just-IN manuscript is the accepted manuscript prior to copy editing and page composition. It may differ from the final official version of record.

Strain response

In Fig. 8, the normal strains in the intermediate (ε_2) and minor (ε_3) principal stress directions are plotted versus ε_1 for each of the three silt-clay soils tested. In this figure, compressive strains are taken as being positive. For all three soils, the intermediate principal strains measured in the undrained true triaxial tests with b = 0.0 were exclusively dilative. As b is increased, the ε_2 values increase (i.e., become less negative), indicating less dilative response. For b = 0.4, the ε_2 values become essentially zero, implying plane strain conditions. For b values greater than 0.4, the intermediate principal strains become compressive.

Regardless of the amount of non-plastic silt present in the soils tested, the minor principal strains remained dilative for all values of b. For all three soils tested, the magnitude of ε_3 increased with increasing values of b. For a given value of b, the intermediate principal strains become slightly less compressive and the minor principal strains become less dilative with increasing silt content, particularly prior to failure.

Undrained moduli

The values of the undrained moduli are determined from plots of $(\sigma_1 - \sigma_3)/\sigma'_c$, versus ε_1. The initial tangent modulus determined within an ε_1 range of 0.2% is denoted by E_0. The secant modulus corresponding to a principal stress difference that is 50% of the maximum value and the corresponding major principal strain ($\varepsilon_{1\ 50}$) is denoted by E_{50}. Fig. 9 presents the variations of normalized E_0 and E_{50} values as a function of the b value. From this figure, it was determined that for all three silt-clay soils tested, the E_0/σ'_c values were approximately 2.5 to 3 times greater than the E_{50}/σ'_c, irrespective of the value of b. As the silt content is increased, the values of E_0/σ'_c and E_{50}/σ'_c increase by as much as a factor of four.

© The Author(s) or their Institution(s)

Canadian Geotechnical Journal (Author Accepted Manuscript)
Version of Record at: https://doi.org/10.1139/cgj-2022-0246

For personal use only. This Just-IN manuscript is the accepted manuscript prior to copy editing and page composition. It may differ from the final official version of record.

As evident from Fig. 9, in Soils 1 and 2, the largest magnitudes of E_0/σ'_c and E_{50}/σ'_c were found for intermediate values of b. In Soil 3, this trend reverses somewhat, as the maximum values for these normalized moduli were found for smaller and larger b values.

Strength characteristics

Undrained shear strength

In Fig. 10, the undrained shear strength, defined from the maximum stress difference as $s_u = (\sigma_1 - \sigma_3)_{max}/2$ and normalized by σ'_c, is plotted versus b. For all values of b considered in the present study, the undrained shear strength is rather significantly influenced by the silt content. For b = 0.0, the s_u/σ'_c values for Soils 1 to 3 are 0.26, 0.33 and 0.44, respectively. For the intermediate b value of 0.4, these values increase by about 15 to 20%. Then, as b values increase to unity, the s_u/σ'_c gradually decrease.

For Soil 1, the value of s_u/σ'_c corresponding to the axisymmetric extension test (i.e., b = 1.0) is slightly larger than that for axisymmetric compression (i.e., b = 0.0). This is not, however, the case for Soils 2 and 3, where s_u/σ'_c values for b = 1.0 are approximately 10% less than those for b = 0.0.

In Fig. 10, the s_u/σ'_c values for the conventional axisymmetric triaxial compression tests for $\sigma'_c =$ 200, 400 and 500 kPa are also plotted. These values, which are labeled in Fig. 10 as "TXC", are seen to be in good agreement with the values from the true triaxial tests with b = 0.0.

Also shown in Fig. 10 are the Tresca and Mises failure criteria. The Tresca criterion predicts constant shear strength that is independent of σ_2. This criterion is expressed in terms of σ_1 and σ_3 as follows:

$$\frac{\sigma_1 - \sigma_3}{2} = \tau_{max} \quad [3]$$

© The Author(s) or Their Institution(s)

Version of Record at: https://doi.org/10.1139/cgj-2022-0246

For personal use only. This Just-IN manuscript is the accepted manuscript prior to copy editing and page composition. It may differ from the final official version of record.

The Mises failure criterion, on the other hand, accounts for the magnitude of intermediate principal stress. It is expressed in terms of the second invariant of the deviatoric stress tensor, $J_2 = \left((\sigma_1 - \sigma_2)^2 + (\sigma_2 - \sigma_3)^2 + (\sigma_1 - \sigma_3)^2\right)/6$ as follows:

$$\frac{\sqrt{3J_2}}{2} = \tau_{max} \quad [4]$$

In the present study, τ_{max} is taken equal to the undrained shear strength (s_u) of Soils 1, 2 and 3 corresponding to *b* = 0.0. The values of τ_{max} for both the Tresca and Mises total failure criteria are listed in Table 2.

Effective friction angle

Figure 11 shows the variation of effective friction angle φ' with *b* value. The values of φ' are determined from the maximum effective stress ratios as follows:

$$\varphi' = \sin^{-1}\left(\frac{\left(\frac{\sigma'_1}{\sigma'_3}\right)_{max} - 1}{\left(\frac{\sigma'_1}{\sigma'_3}\right)_{max} + 1}\right) \quad [5]$$

Similar to the case of normalized undrained shear strength for the three silt-clay soils tested as part of the present study, the effective friction angles become noticeably higher with increasing silt content. For *b* = 0.0, a change in silt content of 45% (from Soil 1 to Soil 3) results in an increase of φ' value as large as 16 degrees. Such increases in φ' are realized for all *b* values. The magnitude of intermediate principal stress also exhibits strong influence on failure. When *b* increases from 0.0 to 0.4, the effective friction angles increase by about 25%, 20% and 10% for Soils 1, 2 and 3, respectively. For Soil 1, the values of φ' decrease slightly as *b* approaches unity. More significant reductions of φ' with increases in *b* are observed for Soil 2 and Soil 3.

© The Author(s) or their Institution(s)

Canadian Geotechnical Journal (Author Accepted Manuscript)
Version of Record at: https://doi.org/10.1139/cgj-2022-0246

For personal use only. This Just-IN manuscript is the accepted manuscript prior to copy editing and page composition. It may differ from the final official version of record.

Finally, a scatter of less than $\pm 2°$ is present when comparing the experimental friction angles determined from the conventional undrained axisymmetric triaxial tests and true triaxial tests with b = 0.0.

Also shown in Fig. 11 are the Mohr-Coulomb and Lade failure criteria. In the absence of effective cohesion, the Mohr-Coulomb failure criterion can be expressed as follows

[6] $$\frac{\sigma'_1 - \sigma'_3}{\sigma'_1 + \sigma'_3} = \sin \varphi'$$

The Mohr-Coulomb failure criterion is fitted to the failure stresses from the undrained true triaxial tests with b = 0.0.

The more general Lade failure criterion (Lade 1977) includes the influence of σ'_2, thereby rendering curved failure envelopes. It is formulated in terms of the first (I'_1) and third (I'_3) invariants of the effective stress tensor as follows:

[7] $$\left(\frac{I'^3_1}{I'_3} - 27\right)\left(\frac{I'_1}{p_a}\right)^m = \eta_1$$

where $I'_1 = \sigma'_1 + \sigma'_2 + \sigma'_3$, $I'_3 = \sigma'_1\, \sigma'_2\, \sigma'_3$ and p_a is the atmospheric pressure, expressed in the same units as the effective stresses (p_a = 100 kPa in the present study). The quantities m and η_1 are dimensionless model parameters whose values are determined from the experimental results of undrained true triaxial tests or conventional triaxial tests (Lade 1977). The values of m and η_1 for the three soils tested in the present study are listed in Table 2.

Total failure surfaces

In Fig. 12, the principal total stresses corresponding to the maximum principal stress differences measured in the true triaxial tests are plotted in the octahedral plane for each of the three soils. Material isotropy is assumed and the experimental stress points are projected based on symmetry about the principal stress axes from the first sector into the other five sectors of the octahedral plane. For comparison, traces of the Tresca and the Mises failure criteria are also

© The Author(s) or their Institution(s)

Version of Record at: https://doi.org/10.1139/cgj-2022-0246

For personal use only. This Just-IN manuscript is the accepted manuscript prior to copy editing and page composition. It may differ from the final official version of record.

plotted on the same octahedral planes. The shape of the total failure surface for Soil 1 in the octahedral plane is essentially circular. When the amount of non-plastic silt is increased, the failure surfaces for Soils 2 and 3 expand and their shapes become slightly more triangular. Curvature of the experimental failure surfaces on octahedral planes indicates strong influence of σ_2 on the total-stress failure characteristics of the tested silt-clay soils. In general, the Tresca failure criterion underpredicts the undrained shear strength, as its hexagonal traces are circumscribed by the experimental failure surfaces. The Mises criterion agrees fairly well with the experimental failure surface of Soil 1, while slightly overpredicting the strength of Soils 2 and 3, particularly for b values greater than 0.4. These trends are also evident in Fig. 10, to which the traces of the Tresca and Mises failure criteria have been added.

Effective failure surfaces

In Fig. 13, the principal effective stresses at failure are projected onto the octahedral plane for each of the three soils tested in the present study. For comparison, traces of the Mohr-Coulomb and Lade failure criteria are plotted on the same octahedral planes (the former are represented by a dotted line; the latter by a solid line).

From Fig. 13, it is evident that the effective failure surfaces for the three silt-clay soils are rounded triangles. Such curved failure surfaces highlight the effect of σ'_2 on the soils' failure. Similar to the total stress failure envelopes, the amount of non-plastic silt contained in a soil affects the effective stress failure envelopes. Increases in the silt content cause the effective failure surfaces to become larger in size and more sharply triangular in shape. This indicates higher shear strengths, which are attributed to increased interlocking between silt particles as the silt content increases.

As evident from Fig. 13, since the Mohr-Coulomb failure criterion is independent of σ'_2, it tends to underpredict the experimental effective stresses at failure rather significantly for all b values except 0.0.

© The Author(s) or their Institution(s)

Canadian Geotechnical Journal (Author Accepted Manuscript)
Version of Record at: https://doi.org/10.1139/cgj-2022-0246

For personal use only. This Just-IN manuscript is the accepted manuscript prior to copy editing and page composition. It may differ from the final official version of record.

By contrast, the predictions made with the more general Lade failure criterion are in excellent agreement with the observed strength for Soil 1 and Soil 2. For Soil 3, the Lade criterion overpredicts the experimental failure stresses, particularly for all b values except zero and unity. These trends are also evident for the case of φ' from Fig. 11, to which the traces of the Mohr-Coulomb and Lade failure criteria have been added.

Directions of plastic strain increment vectors

Knowledge of the variation in the direction of plastic strain increment vector during loading is instrumental to modeling the stress-strain behavior of soils within the framework of elastoplasticity theory. Assuming an additive decomposition of the total strain increment vector ($d\varepsilon_i$) into an elastic ($d\varepsilon_i^e$) and a plastic part ($d\varepsilon_i^p$), the incremental plastic strain is determined as follows: $d\varepsilon_i^p = d\varepsilon_i - d\varepsilon_i^e$. Here i = 1, 2, 3 signify the principal directions. In the present study, the total strain increment vectors were obtained directly from the results of the true triaxial tests with different b values and from the conventional axisymmetric triaxial compression tests with different values of σ'_c.

The elastic strain increments are computed from the experimental effective stress increments based on elasticity theory. The elastic stress-strain response is assumed to be isotropic. In terms of the increments of principal effective stress, this response is written as follows:

[8] $$\begin{Bmatrix} d\varepsilon_1^e \\ d\varepsilon_2^e \\ d\varepsilon_3^e \end{Bmatrix} = \frac{1}{E}\begin{bmatrix} 1 & -\nu & -\nu \\ -\nu & 1 & -\nu \\ -\nu & -\nu & 1 \end{bmatrix}\begin{Bmatrix} d\sigma'_1 \\ d\sigma'_2 \\ d\sigma'_3 \end{Bmatrix}$$

In Eq. 8, E is Young's modulus and ν is Poisson's ratio. Past experimental studies have indicated strong dependency of the elastic or unload-reload response of cohesive soils on the state of stress. In general, high levels of both effective mean stress and deviatoric stress render larger magnitudes of elastic Young's, bulk and shear moduli. To reflect such stress-dependent

© The Author(s) or their Institution(s)

Version of Record at: https://doi.org/10.1139/cgj-2022-0246

For personal use only. This Just-IN manuscript is the accepted manuscript prior to copy editing and page composition. It may differ from the final official version of record.

behavior, the isotropic elastic model proposed by Lade and Nelson (1987) is employed to compute the value of Young's modulus; i.e.,

$$E = Mp_a\left[\left(\frac{I'_1}{p_a}\right)^2 + 6\left(\frac{1+\nu}{1-2\nu}\right)\frac{J_2}{p_a^2}\right]^\lambda \qquad [9]$$

where I'_1, J_2 and p_a are as previously defined and M and λ are dimensionless model parameters. The value of ν is assumed to be constant. Thus, only is E taken as stress dependent. Following the procedure described by Lade and Nelson (1987), the values of ν, M and λ were determined from the stress-strain and volume change relations during unload-reload cycles of a series of consolidated-drained axisymmetric triaxial compression tests on normally consolidated specimens of the three silt-clay soils (Anantanasakul and Roth 2015). Table 2 lists the values of the isotropic elastic model parameters (ν, M and λ) for the three soils tested in the present study.

The principal strain increment axes are superimposed on the principal stress axes. In Fig. 14, the directions of plastic strain increment vectors obtained from the undrained true triaxial tests are plotted in the octahedral planes at the corresponding stress points from which these vectors are determined. As evident from Fig. 14, for b = 0.0, the directions of plastic strain increment vectors on the octahedral planes coincide with the rectilinear stress path associated with this test. As the value of b is increased, these vectors progressively rotate in a clockwise manner until eventually coinciding with the stress paths for the b = 1.0 test. Such clockwise orientation of the plastic strain increment vectors from the stress paths for intermediate b values appears to be more pronounced when the amount of non-plastic silt in the soil is increased.

In Fig. 15, the incremental plastic strain vectors obtained from the axisymmetric triaxial compression tests are plotted in the triaxial plane. For brevity, only results for the three values of σ'_c associated with Soil 1 are plotted in Fig. 15. At the end of consolidation, the strain vectors are aligned with the hydrostatic axis. Following the onset of shearing, these vectors rotate in a

© The Author(s) or their Institution(s)

Version of Record at: https://doi.org/10.1139/cgj-2022-0246

For personal use only. This Just-IN manuscript is the accepted manuscript prior to copy editing and page composition. It may differ from the final official version of record.

counterclockwise manner, eventually forming angles that are slightly less than 90 degrees from the hydrostatic axis.

At failure, there are essentially no changes in the effective stresses. Consequently, the elastic strain increments remain unchanged. Since volume change, in terms of total strain increments, is zero during undrained shearing, it follows that there will be no change in the plastic volumetric strain. The plastic strain increment vectors at failure should thus be perpendicular to the hydrostatic axis. In Fig. 15, this is seen to be the case for Soil 1. Similar trends for the plastic strain increment vectors in the triaxial plane are observed for Soils 2 and 3 (but are omitted for brevity).

According to hardening elastoplasticity theory, the direction of plastic strain increment vector is computed by assuming normality to the plastic potential surface. It is thus instructive to investigate the possible shapes of this surface that are suggested by the observed directions of plastic strain increment vectors from the true triaxial tests that were performed on the silt-clay soils. As shown in Fig. 14, the traces of the plastic potential function in the octahedral planes are approximately similar to those of the failure surfaces, being rounded triangles in shape, even at early stages of shearing. From the results of the aforementioned tests, it is evident that the shapes of plastic potential surfaces become more sharply triangular with increasing silt content. From Fig. 15, it is evident that traces of the plastic potential function in the triaxial plane are shaped like flattened ellipses or "cigars" with rounded tips that coincide with the hydrostatic axis. As the amount of non-plastic silt is increased, the plastic strain increment vectors become more sharply oriented in a counterclockwise direction. Consequently, the corresponding shapes of plastic potential surfaces in the triaxial plane become flatter with more pointed tips.

The benefit of computing and presenting the plastic strain increment vectors shown in Figs. 14 and 15 is that individuals that mathematically model the response of silt-clay transition soils

© The Author(s) or their Institution(s)

Version of Record at: https://doi.org/10.1139/cgj-2022-0246

For personal use only. This Just-IN manuscript is the accepted manuscript prior to copy editing and page composition. It may differ from the final official version of record.

can assess the accuracy of their model for computing strain increments. This, in turn, provides a means by which the need for using a non-associative flow rule can be rationally assessed.

Conclusions

The experimental study presented in this paper investigated the effects of silt content and magnitude of intermediate principal stress on the stress-strain, excess pore pressure and strength behavior of silt-clay transition soils. Undrained true triaxial tests with constant b values were performed on normally consolidated specimens of silt-clay soils created from the same base clay and non-plastic silt but with systematically varying gradations. It was observed from the experimental results that with increasing amount of non-plastic silt, the transition soils clearly exhibited stiffer stress-strain response as indicated by higher values of undrained modulus evaluated at different levels of strain. For b values of 0.2 and less, the silt-clay soils showed smooth stress-strain curves up to large strains. For higher b values, the stress-strain curves corresponded to be more “brittle” behavior. That is, they increased sharply to reach failure at smaller major principal strains. The peak values of principal stress difference were often followed by significant reductions in strength.

Under three-dimensional stress conditions, the normally consolidated soils exhibited overall contractive tendency during shear. Regardless of b value, the pore pressure changes increased more sharply to reach higher maximum values as the silt content was increased. When the effect of change in principal stresses was considered, less contractive tendencies, as determined by smaller values of the Henkel and Wade pore pressure parameter corresponding to the maximum principal stress difference ($\bar{a}_f$), were observed.

For all b values considered, the undrained shear strengths and effective friction angles of the silt-clay transition soils were observed to significantly increase with the amount of silt. The strength values also increased by as much as 25% as b increased from 0.0 to the intermediate

© The Author(s) or their Institution(s)

Canadian Geotechnical Journal (Author Accepted Manuscript)
Version of Record at: https://doi.org/10.1139/cgj-2022-0246
For personal use only. This Just-IN manuscript is the accepted manuscript prior to copy editing and page composition. It may differ from the final official version of record.

value of 0.4. The shear strengths and friction angles then gradually decreased as *b* values increased toward unity.

Curved total and effective failure surfaces in octahedral planes were observed for all cohesive soils, clearly suggesting the influence of intermediate principal stress on failure. With increasing silt content, both the total and effective stress failure surfaces expanded and their shapes became more sharply triangular. Such observations signify higher shear strengths and more pronounced frictional response of the tested soils, possibly due to interparticle friction among the silt grains that are in greater contact with one another with increasing silt content.

Traces of the plastic potential function in the octahedral plane were observed to be approximately similar to those of the failure surfaces, being rounded triangles in shape, even in the early stages of shearing. The shapes of plastic potential surfaces clearly changed, becoming more sharply triangular with increasing silt content. Traces of the plastic potential function in the triaxial plane were observed to be flattened ellipses or "cigar-like" in shape with rounded tips on the hydrostatic axis. As the amount of non-plastic silt in the soils increased, the shapes of plastic potential surfaces in the triaxial plane became flatter with more pointed tips.

Acknowledgement

Funding for this study was provided by the Thailand Research Fund (TRF) through Grant TRG5780237. The authors wish to thank Mr. Gong Chaosittichai, former Graduate Assistant of the Geotechnical Engineering Laboratory at Mahidol University, for his assistance in fabrication of the true triaxial apparatus presented herein.

Competing interests: The authors declare there are no competing interests.

Data availability: Data generated or analyzed during this study are provided in full within the published article.

© The Author(s) or their Institution(s)

Version of Record at: https://doi.org/10.1139/cgj-2022-0246

For personal use only. This Just-IN manuscript is the accepted manuscript prior to copy editing and page composition. It may differ from the final official version of record.

References

Anantanasakul, P., and Roth, C. 2015. Mechanical behavior of silt-clay transition soils. In Proceedings of the International Conference on Soft Ground Engineering, Singapore, 3-5 December 2015. Geotechnical Society of Singapore, Singapore, 1(1): 483-493.

Anantanasakul, P., and Roth, C. 2018. Undrained behavior of silt-clay transition soils with varying degrees of overconsolidation. Journal of GeoEngineering, 13(1): 1-12.

Anantanasakul, P., Yamamuro, J., and Kaliakin, V.N. 2012a. Stress-strain and strength characteristics of silt-clay transition soils. Journal of Geotechnical and Geoenvironmental Engineering, 138(10): 1257-1265.

Anantanasakul, P., Yamamuro, J., and Lade, P.V. 2012b. Three-dimensional drained behavior of normally consolidated anisotropic kaolin clay. Soils and Foundation, 52(1): 146-159.

Bishop, A.W., and Henkel, D.J. 1957. The triaxial test. Edward Arnold Publishers, London.

Boulanger, R.W., and Idriss, I.M. 2006. Liquefaction susceptibility criteria for silts and clays. Journal of Geotechnical and Geoenvironmental Engineering, 132(11): 1413-1426.

Cola, S., and Simonini, P. 2002. Mechanical behavior of silty soils of the Venice lagoon as a function of their grading characteristics. Canadian Geotechnical Journal, 39(4): 879-893.

Ferreira, P.M., and Bica, A.V.D. 2006. Problems in identifying the effects of structure and critical state in soil with transitional behavior. Géotechnique, 56(7): 445-454.

Henkel, D.J., and Wade, N.H. 1966. Plane strain tests on a saturated remolded clay. Journal of the Soil Mechanics and Foundations Division ASCE, 92(6): 67-80.

Kirkgard, M.M., and Lade, P.V. 1993. Anisotropic three-dimensional behavior of a normally consolidated clay. Canadian Geotechnical Journal, 30(4): 848-858.

Lade, P.V. 1977. Elasto-plastic stress-strain theory for cohesionless soil with curved yield surfaces. International Journal of Solids and Structures, 13(11): 1019-1035.

© The Author(s) or their Institution(s)

Canadian Geotechnical Journal (Author Accepted Manuscript)
Version of Record at: https://doi.org/10.1139/cgj-2022-0246
For personal use only. This Just-IN manuscript is the accepted manuscript prior to copy editing and page composition. It may differ from the final official version of record.

Lade, P.V. 1988. Automatic volume change and pressure measurement devices for triaxial testing of soils. ASTM Geotechnical Testing Journal, 11(4): 263-268.

Lade, P.V. 2003. Analysis and prediction of shear banding under 3D conditions in granular materials. Soils and Foundations, 43(4): 161-172.

Lade, P.V. 2016. Triaxial testing of soils. John Wiley & Sons, Chichester.

Lade, P.V., and Nelson, R.B. 1987. Modeling the elastic behavior of granular materials. International Journal for Numerical and Analytical Methods in Geomechanics, 11(5): 521-542.

Lade, P.V., Jungman, N., and Hong, W.P. 2008. Shear banding and cross-anisotropic behavior observed in laboratory sand tests with stress rotation. Canadian Geotechnical Journal, 45(1): 74-84.

Matsuoka, H., Sun, D., Kogane, A., Fukuzawa, N., and Ichihara, W. 2002. Stress-strain behavior of unsaturated soil in true triaxial tests. Canadian Geotechnical Journal, 39(3): 608-619.

Nakai, T., Matsuoka, H., Okuno, N., and Tsuzuki, K. 1986. True triaxial tests on normally consolidated clay and analysis of the observed shear behavior using elastoplastic constitutive models. Soils and Foundations, 26(4): 67-78.

Nocilla, A., Coop, M.R., and Colleselli, F. 2006. The mechanics of an Italian silt: an example of ‘transitional’ behavior. Géotechnique, 56(4): 261-271.

Prashant, A., and Penumadu, D. 2005. A laboratory study of normally consolidated kaolin clay. Canadian Geotechnical Journal, 42(1): 27-37.

Rudnicki, J.W., and Rice, J.R. 1975. Conditions for localization of deformation in pressure-sensitive dilatant materials. Journal of the Mechanics and Physics of Solids, 23(6): 371-394.

Skempton, A.W. 1954. The pore pressure coefficients A and B. Géotechnique, 4(4): 143-147.

© The Author(s) or their Institution(s)

Version of Record at: https://doi.org/10.1139/cgj-2022-0246

For personal use only. This Just-IN manuscript is the accepted manuscript prior to copy editing and page composition. It may differ from the final official version of record.

Vadoulakis, I. 1996. Deformation of water-saturated sand: I uniform undrained deformation and shear banding. Geotechnique, 43(3): 441-456.

Vermeer, P.A. 1982. A simple shear band analysis using compliance. In Proceedings of the International Union of Theoretical and Applied Mechanics Symposium on Deformation and Failure of Granular Materials, Delft, The Netherlands, 21 August – 3 September 1992. 1(1): 493-499.

Wang, Q., and Lade, P.V. 2001. Analysis of shear banding in true triaxial tests on sand. Journal of Engineering Mechanics, 127(8): 762-768.

Wang, S., and Luna, R. 2012. Monotonic behavior of Mississippi River Valley silt in triaxial compression. Journal of Geotechnical and Geoenvironmental Engineering, 138(4): 516-525.

Wong, S.T.Y., Ong, D.E.L., and Robinson, R.G. 2017. Behavior of MH silts with varying plasticity indices. Geotechnical Research, 4(2): 118-135.

Yin, J.H. 1999. Properties and behavior of Hong Kong marine deposits with different clay contents. Canadian Geotechnical Journal, 36(6): 1085-1095.

Yin, J.H. 2002. Stress-strain strength characteristics of a marine soil with different clay contents. ASTM Geotechnical Testing Journal, 25(4): 459-462.

Yin, J.H., Cheng, C.M., Kumruzzaman, M., and Zhou, W.H. 2010. New mixed boundary, true triaxial loading device for testing three-dimensional stress-strain-strength behavior of geomaterials. Canadian Geotechnical Journal, 47(1): 1-15.

© The Author(s) or their Institution(s)

Canadian Geotechnical Journal (Author Accepted Manuscript)
Version of Record at: https://doi.org/10.1139/cgj-2022-0246
For personal use only. This Just-IN manuscript is the accepted manuscript prior to copy editing and page composition. It may differ from the final official version of record.

Figure Captions

Fig. 1. Particle-size distribution for tested silt-clay soils. Gradation curve of non-plastic silt is plotted for comparison.

Fig. 2. Scanning electron micrographs at a magnification of 1000.

Fig. 3. True triaxial apparatus: (a) cutaway view of cell and (b) photograph of prismatic soil specimen and horizontal loading system.

Fig. 4. Stress differences, effective stress ratios, pore pressure changes versus major principal strains for b values of 0.0, 0.1, 0.2 and 0.4.

Fig. 5. Stress differences, effective stress ratios, pore pressure changes versus major principal strains for b values of 0.6, 0.8, 0.9 and 1.0.

Fig. 6. Shear band developed in prismatic specimen. Shear band offset is visible on σ_3 side of specimen.

Fig. 7. Variation of values of Henkel-Wade pore pressure parameter a¯_f versus b values.

Fig. 8. Intermediate and minor principal strains versus major principal strains.

Fig. 9. Variation of values of initial tangent modulus and secant modulus evaluated at 50% of maximum stress differences normalized with effective consolidation pressures with b values.

Fig. 10. Variation of undrained shear strengths normalized by effective consolidation pressures versus b values. Predictions by Mises and Tresca failure criteria are also plotted for comparison.

Fig. 11. Variation of effective friction angles versus b values. Predictions by Mohr-Coulomb and Lade failure criteria are also plotted.

Fig. 12. Total stress failure surfaces in octahedral planes. Mises and Tresca failure surfaces corresponding to undrained shear strengths of b = 0.0 tests are also plotted.

Fig. 13. Effective stress failure surfaces in octahedral planes. Mohr-Coulomb and Lade failure surfaces corresponding to strengths of b = 0.0 tests are also plotted.

© The Author(s) or their Institution(s)

Version of Record at: https://doi.org/10.1139/cgj-2022-0246

For personal use only. This Just-IN manuscript is the accepted manuscript prior to copy editing and page composition. It may differ from the final official version of record.

Fig. 14. Directions of plastic strain increment vectors projected on octahedral planes.

Fig. 15. Directions of plastic strain increment vectors in triaxial plane for triaxial compression tests (b = 0.0) and true triaxial extension (b = 1.0) test on Soil 1.

© The Author(s) or their Institution(s)

Canadian Geotechnical Journal (Author Accepted Manuscript)
Version of Record at: https://doi.org/10.1139/cgj-2022-0246

For personal use only. This Just-IN manuscript is the accepted manuscript prior to copy editing and page composition. It may differ from the final official version of record.

Table 1. Clay, silt, sand contents and properties of tested silt-clay soils.

Soil property	Soil 1	Soil 2	Soil 3
Amount of base clay in mixture (%)	100	57	29
Amount of non-plastic silt in mixture (%)	0	43	71
Clay content (%)	74	49	30
Silt content (%)	24	50	69
Sand content (%)	2	1	1
Liquid limit	55	42	30
Plastic limit	35	31	24
Plasticity index	20	11	6
USCS classification	MH	ML	ML
Specific gravity	2.64	2.64	2.65
Skempton's activity coefficient	0.27	0.22	0.20
Water content of sample (%)	38	29	23
Initial void ratio of sample	0.95	0.77	0.65
Unit weight of sample (kN/m^3)	18.34	18.84	19.42

© The Author(s) or their Institution(s)

Version of Record at: https://doi.org/10.1139/cgj-2022-0246

For personal use only. This Just-IN manuscript is the accepted manuscript prior to copy editing and page composition. It may differ from the final official version of record.

Table 2. Parameter values for Tresca, Mises, Mohr-Coulomb, and Lade failure criteria and Lade-Nelson elastic model.

Criterion and model	Model parameter	Soil 1	Soil 2	Soil 3
Tresca	τ_{max} (kPa)	51	67	87
Mises	τ_{max} (kPa)	51	67	87
Mohr-Coulomb	φ' ($b = 0.0$) (deg)	21.27	27.97	37.64
Lade	m	0.44	0.30	0.16
	η_1	7.24	12.02	26.30
Lade-Nelson elastic model	ν	0.21	0.29	0.34
	M	25	100	300
	λ	0.72	0.41	0.33

© The Author(s) or their Institution(s)

Canadian Geotechnical Journal (Author Accepted Manuscript)
Version of Record at: https://doi.org/10.1139/cgj-2022-0246

For personal use only. This Just-IN manuscript is the accepted manuscript prior to copy editing and page composition. It may differ from the final official version of record.

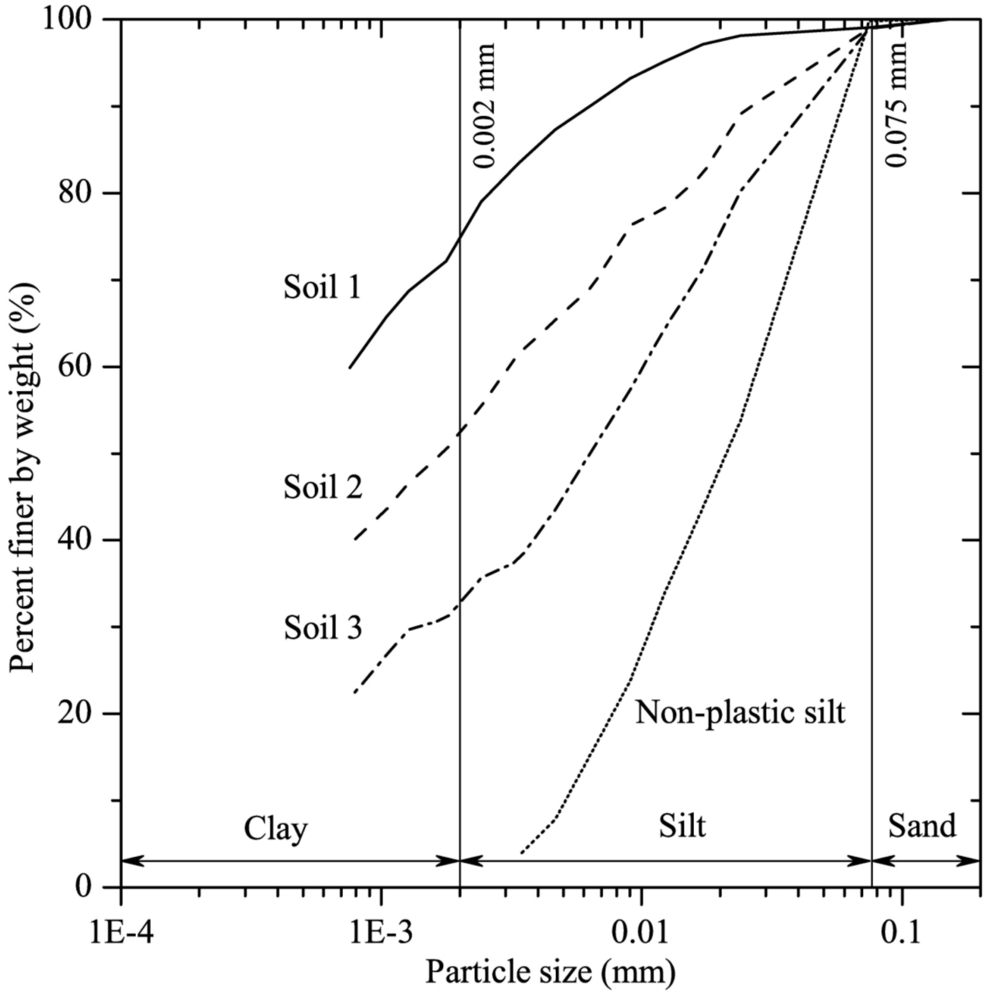

Fig. 1. Particle-size distribution for tested silt-clay soils. Gradation curve of non-plastic silt is plotted for comparison.

166x167mm (300 x 300 DPI)

© The Author(s) or their Institution(s)

Version of Record at: https://doi.org/10.1139/cgj-2022-0246

For personal use only. This Just-IN manuscript is the accepted manuscript prior to copy editing and page composition. It may differ from the final official version of record.

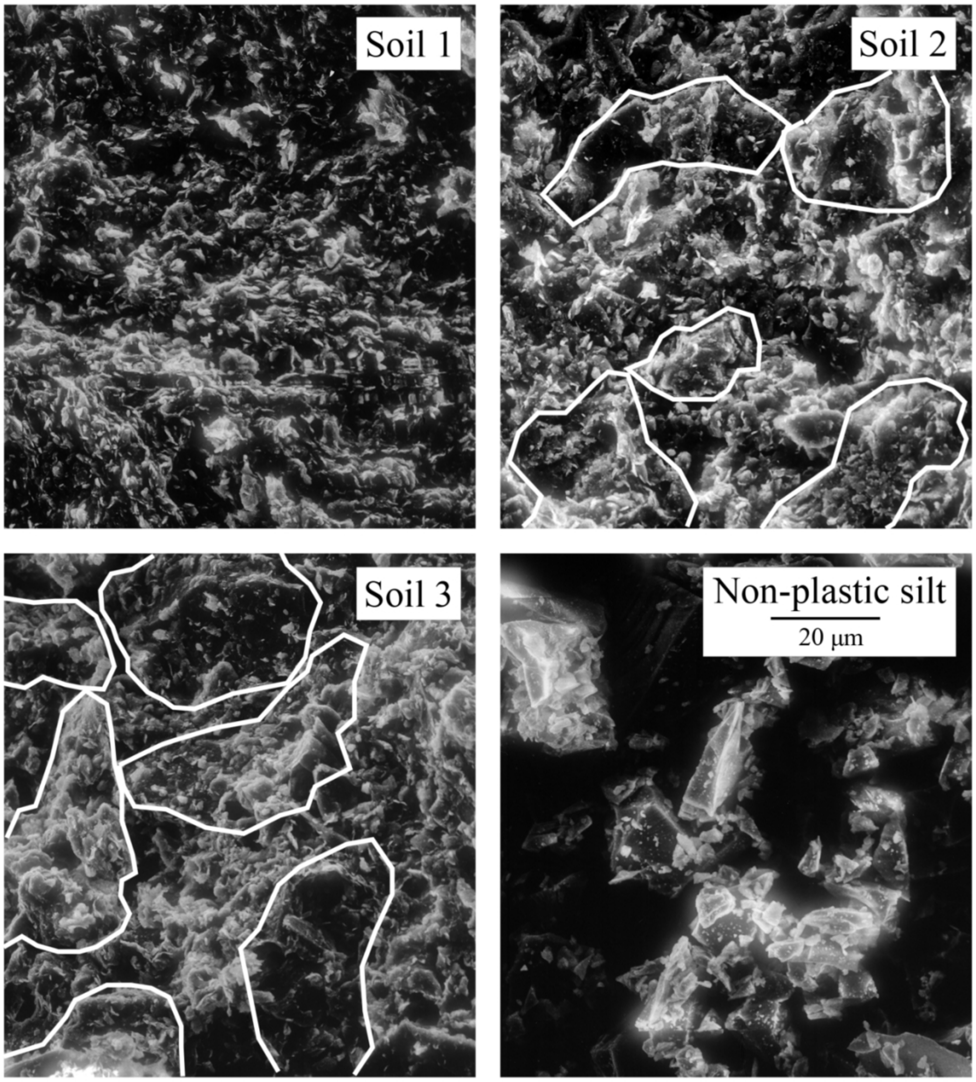

Fig. 2. Scanning electron micrographs at a magnification of 1000.

111x122mm (300 x 300 DPI)

© The Author(s) or their Institution(s)

Canadian Geotechnical Journal (Author Accepted Manuscript)
Version of Record at: https://doi.org/10.1139/cgj-2022-0246

For personal use only. This Just-IN manuscript is the accepted manuscript prior to copy editing and page composition. It may differ from the final official version of record.

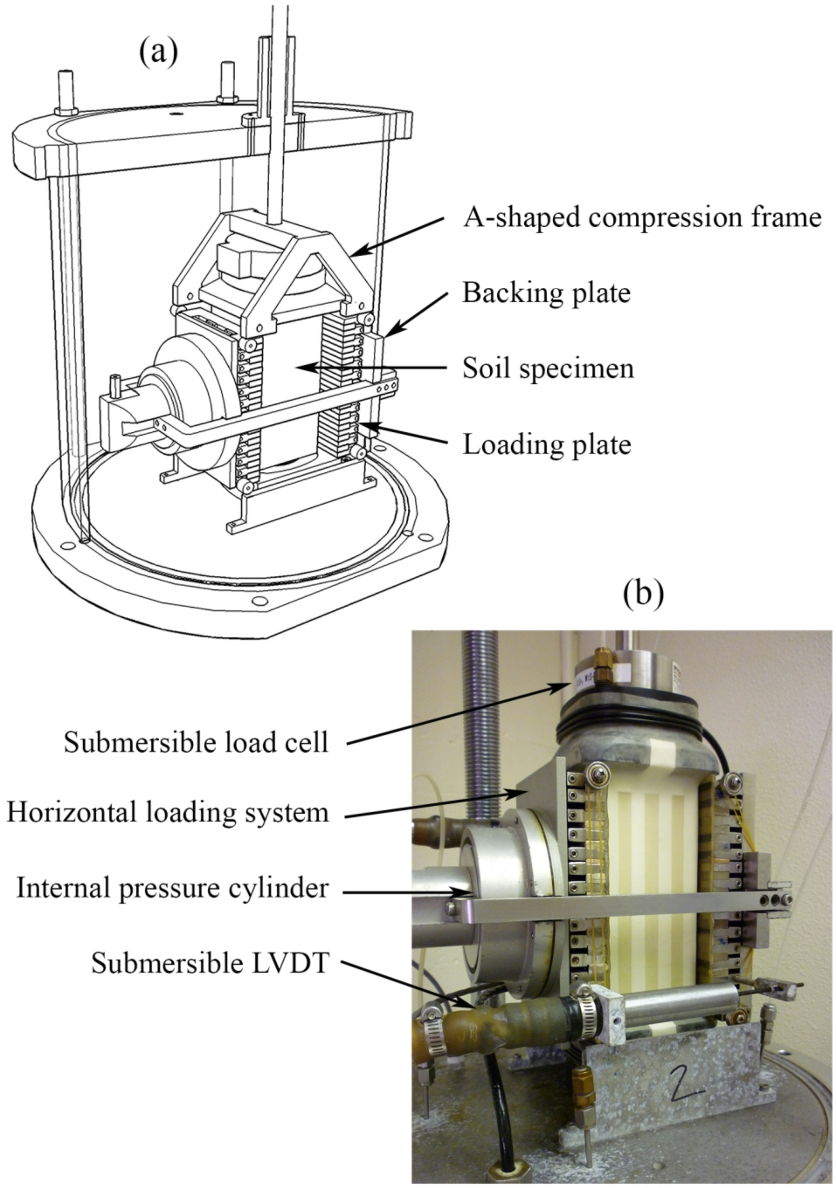

Fig. 3. True triaxial apparatus: (a) cutaway view of cell and (b) photograph of prismatic soil specimen and horizontal loading system.

119x169mm (300 x 300 DPI)

© The Author(s) or their Institution(s)

Version of Record at: https://doi.org/10.1139/cgj-2022-0246

For personal use only. This Just-IN manuscript is the accepted manuscript prior to copy editing and page composition. It may differ from the final official version of record.

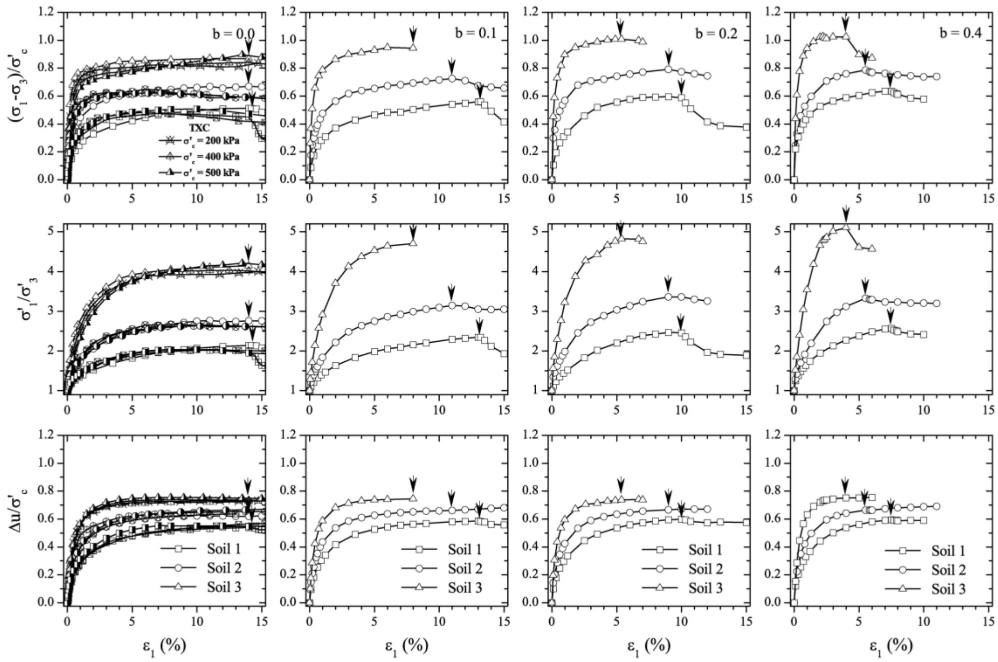

Fig. 4. Stress differences, effective stress ratios, pore pressure changes versus major principal strains for b values of 0.0, 0.1, 0.2 and 0.4.

247x163mm (300 x 300 DPI)

© The Author(s) or their Institution(s)

Version of Record at: https://doi.org/10.1139/cgj-2022-0246

For personal use only. This Just-IN manuscript is the accepted manuscript prior to copy editing and page composition. It may differ from the final official version of record.

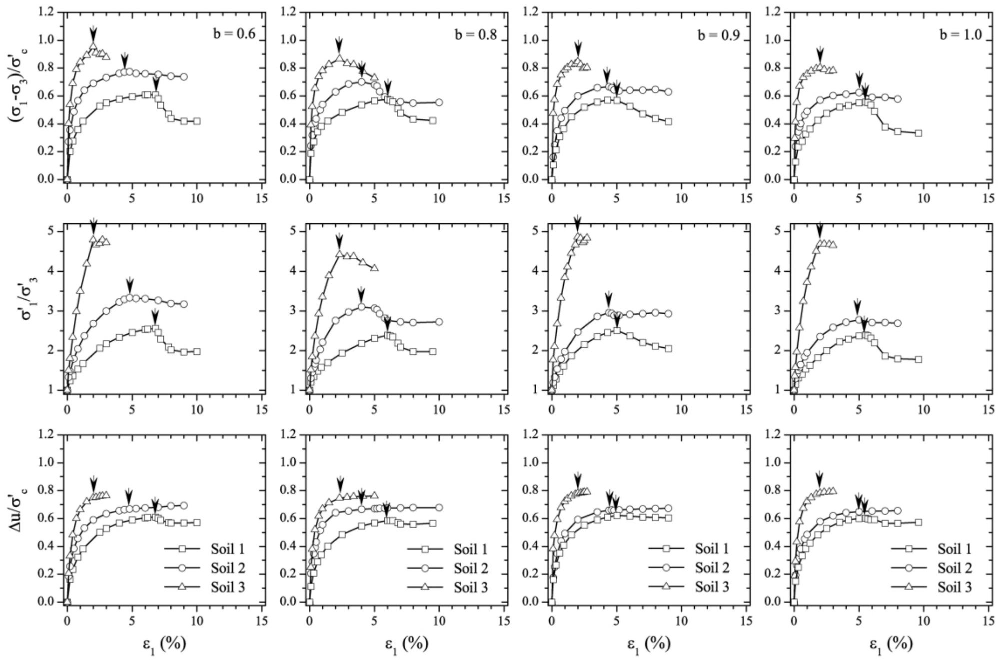

Fig. 5. Stress differences, effective stress ratios, pore pressure changes versus major principal strains for b values of 0.6, 0.8, 0.9 and 1.0.

247x163mm (300 x 300 DPI)

© The Author(s) or their Institution(s)

Version of Record at: https://doi.org/10.1139/cgj-2022-0246

For personal use only. This Just-IN manuscript is the accepted manuscript prior to copy editing and page composition. It may differ from the final official version of record.

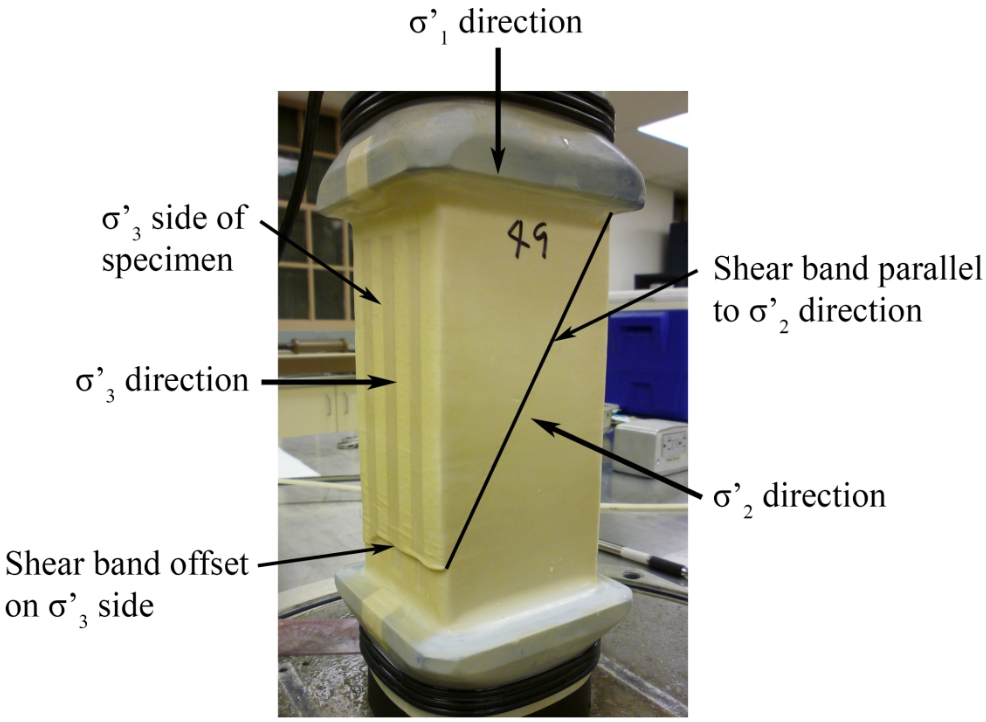

Fig. 6. Shear band developed in prismatic specimen. Shear band offset is visible on σ_3 side of specimen.

199x145mm (300 x 300 DPI)

© The Author(s) or their Institution(s)

Version of Record at: https://doi.org/10.1139/cgj-2022-0246
For personal use only. This Just-IN manuscript is the accepted manuscript prior to copy editing and page composition. It may differ from the final official version of record.

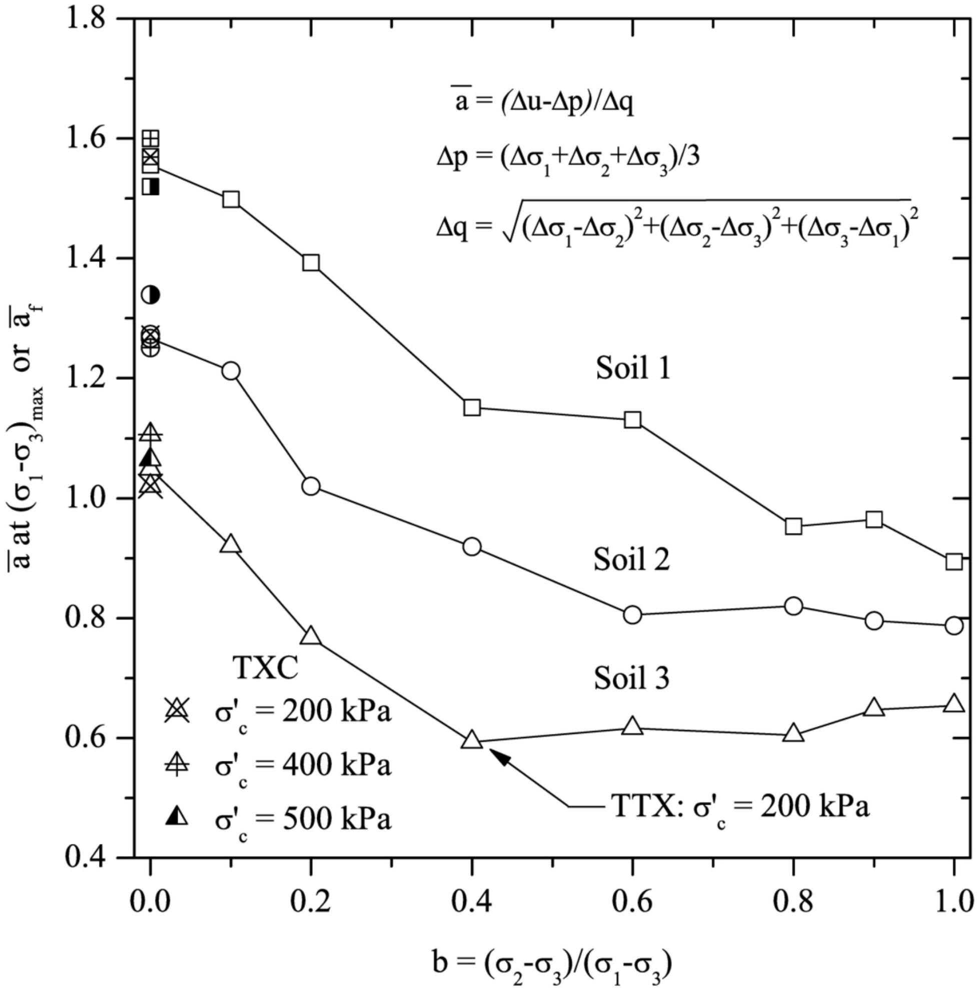

Fig. 7. Variation of values of Henkel-Wade pore pressure parameter a _f versus b values.

172x172mm (300 x 300 DPI)

© The Author(s) or their Institution(s)

Version of Record at: https://doi.org/10.1139/cgj-2022-0246

For personal use only. This Just-IN manuscript is the accepted manuscript prior to copy editing and page composition. It may differ from the final official version of record.

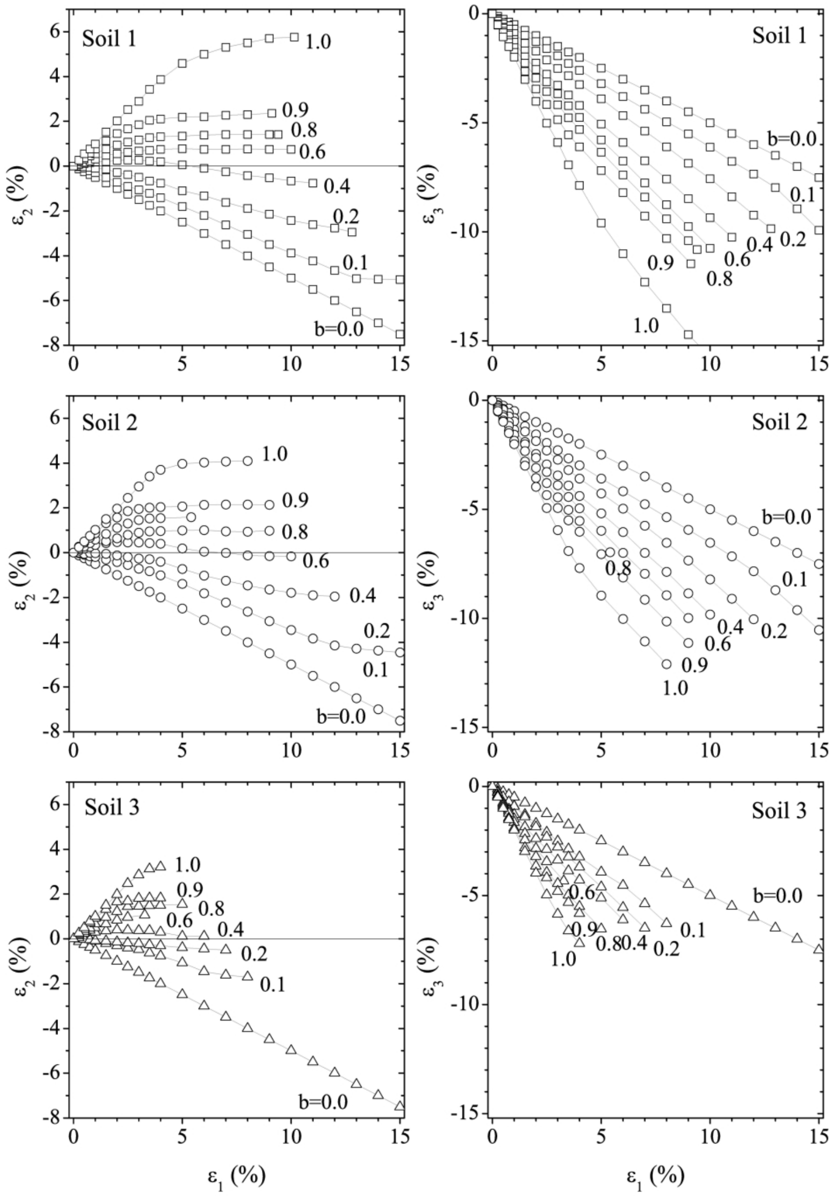

Fig. 8. Intermediate and minor principal strains versus major principal strains.

224x321mm (300 x 300 DPI)

© The Author(s) or their Institution(s)

Version of Record at: https://doi.org/10.1139/cgj-2022-0246
For personal use only. This Just-IN manuscript is the accepted manuscript prior to copy editing and page composition. It may differ from the final official version of record.

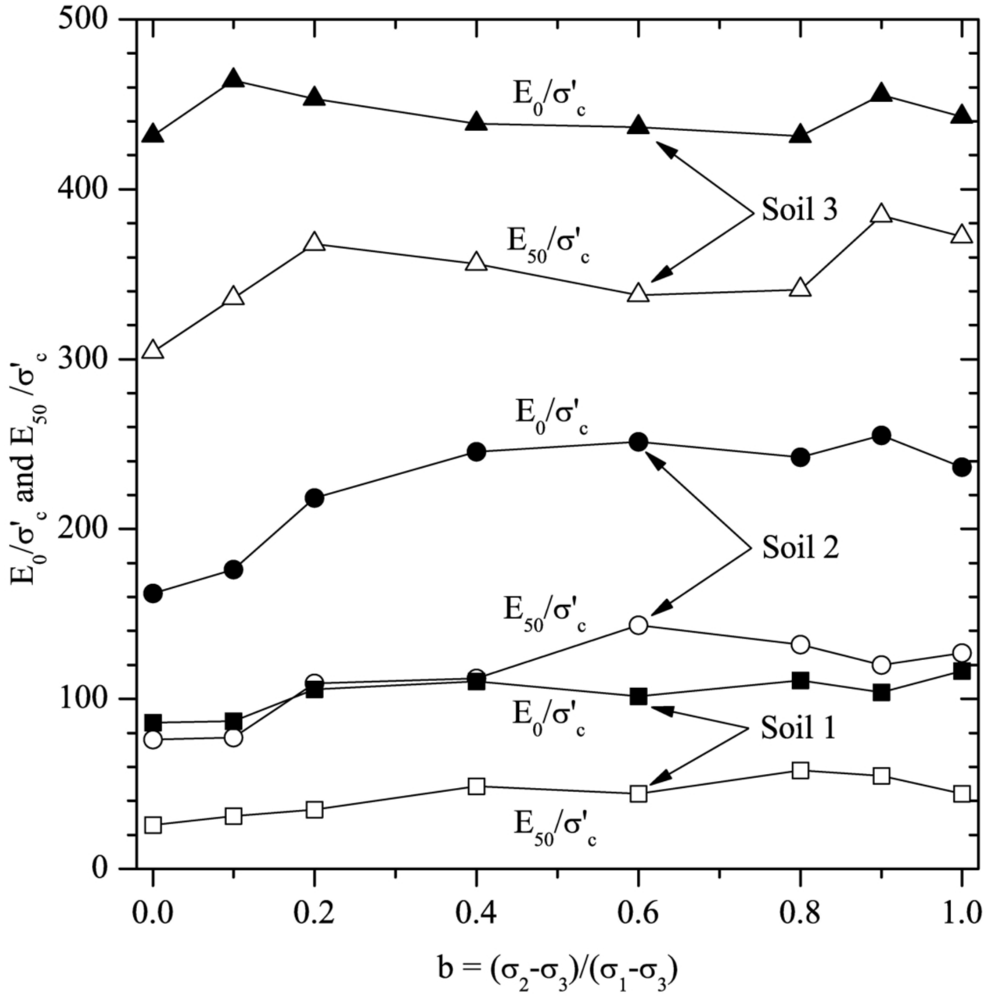

Fig. 9. Variation of values of initial tangent modulus and secant modulus evaluated at 50% of maximum stress differences normalized with effective consolidation pressures with b values.

170x171mm (300 x 300 DPI)

© The Author(s) or their Institution(s)

Version of Record at: https://doi.org/10.1139/cgj-2022-0246
For personal use only. This Just-IN manuscript is the accepted manuscript prior to copy editing and page composition. It may differ from the final official version of record.

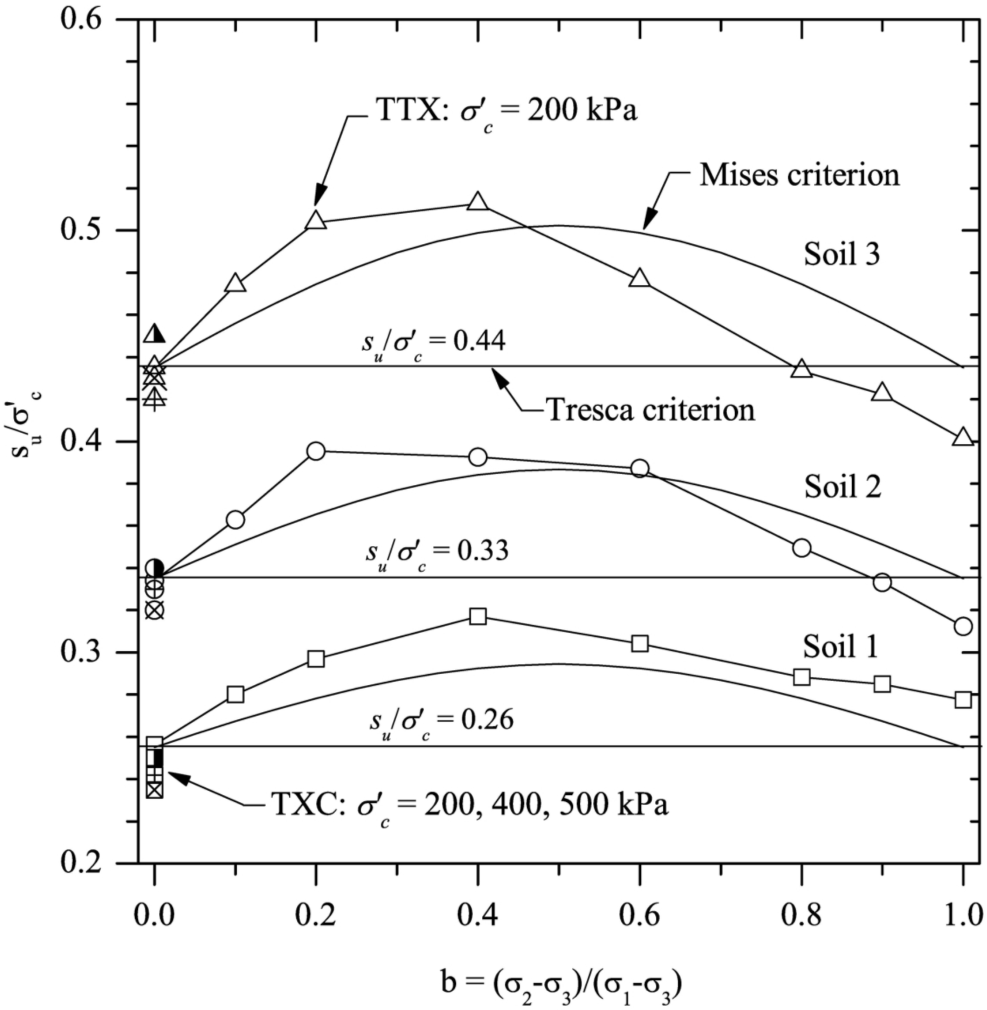

Fig. 10. Variation of undrained shear strengths normalized by effective consolidation pressures versus b values. Predictions by Mises and Tresca failure criteria are also plotted for comparison.

171x175mm (300 x 300 DPI)

© The Author(s) or their Institution(s)

Canadian Geotechnical Journal (Author Accepted Manuscript)
Version of Record at: https://doi.org/10.1139/cgj-2022-0246

For personal use only. This Just-IN manuscript is the accepted manuscript prior to copy editing and page composition. It may differ from the final official version of record.

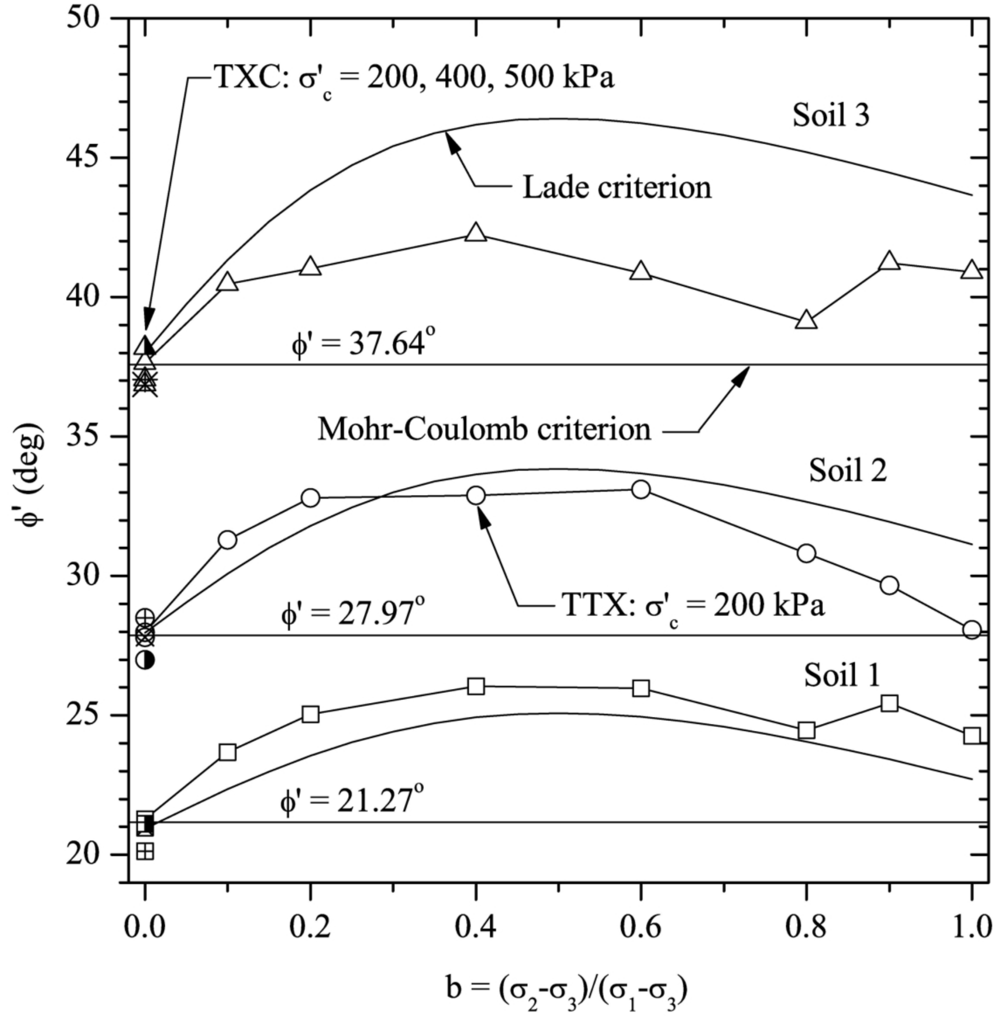

Fig. 11. Variation of effective friction angles versus b values. Predictions by Mohr-Coulomb and Lade failure criteria are also plotted.

169x174mm (300 x 300 DPI)

© The Author(s) or their Institution(s)

Version of Record at: https://doi.org/10.1139/cgj-2022-0246

For personal use only. This Just-IN manuscript is the accepted manuscript prior to copy editing and page composition. It may differ from the final official version of record.

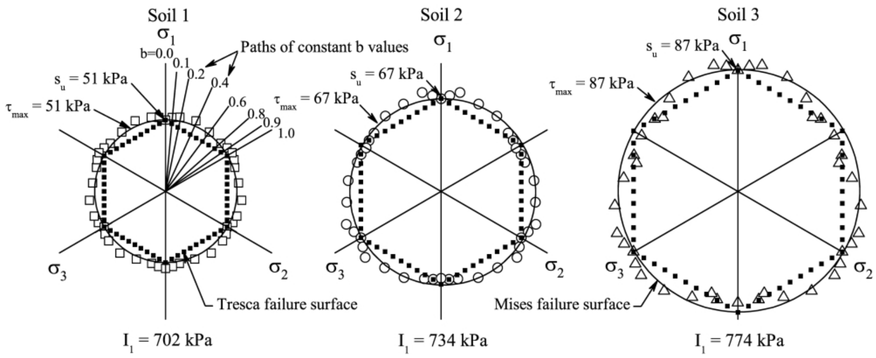

Fig. 12. Total stress failure surfaces in octahedral planes. Mises and Tresca failure surfaces corresponding to undrained shear strengths of b = 0.0 tests are also plotted.

353x151mm (300 x 300 DPI)

© The Author(s) or their Institution(s)

Version of Record at: https://doi.org/10.1139/cgj-2022-0246
For personal use only. This Just-IN manuscript is the accepted manuscript prior to copy editing and page composition. It may differ from the final official version of record.

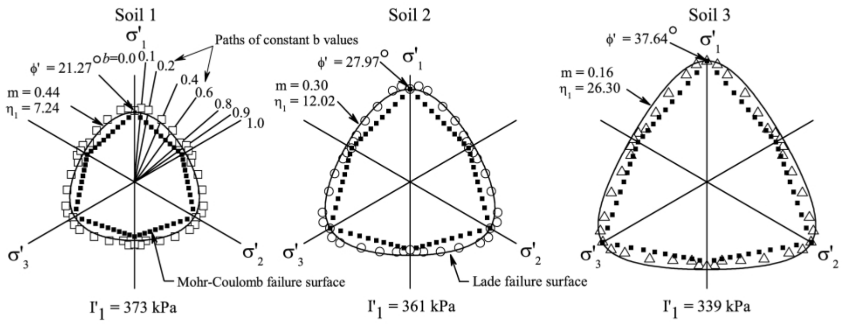

Fig. 13. Effective stress failure surfaces in octahedral planes. Mohr-Coulomb and Lade failure surfaces corresponding to strengths of b = 0.0 tests are also plotted.

353x151mm (300 x 300 DPI)

© The Author(s) or their Institution(s)

Version of Record at: https://doi.org/10.1139/cgj-2022-0246

For personal use only. This Just-IN manuscript is the accepted manuscript prior to copy editing and page composition. It may differ from the final official version of record.

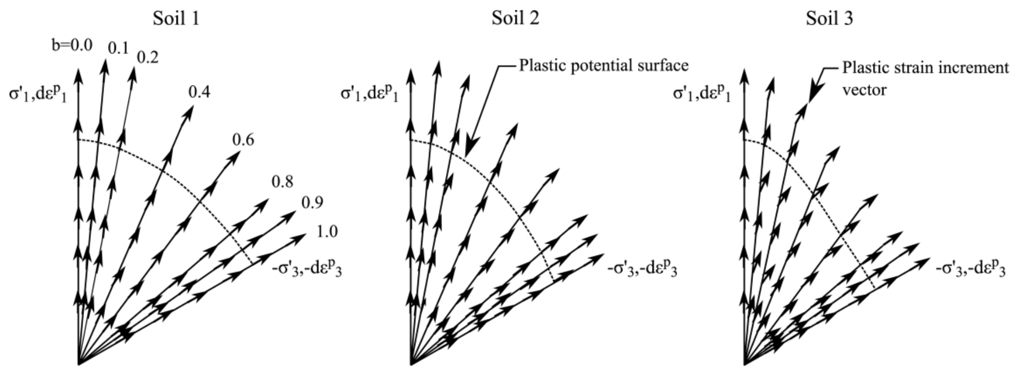

Fig. 14. Directions of plastic strain increment vectors projected on octahedral planes.

515x184mm (300 x 300 DPI)

© The Author(s) or their Institution(s)

Canadian Geotechnical Journal (Author Accepted Manuscript)
Version of Record at: https://doi.org/10.1139/cgj-2022-0246
For personal use only. This Just-IN manuscript is the accepted manuscript prior to copy editing and page composition. It may differ from the final official version of record.

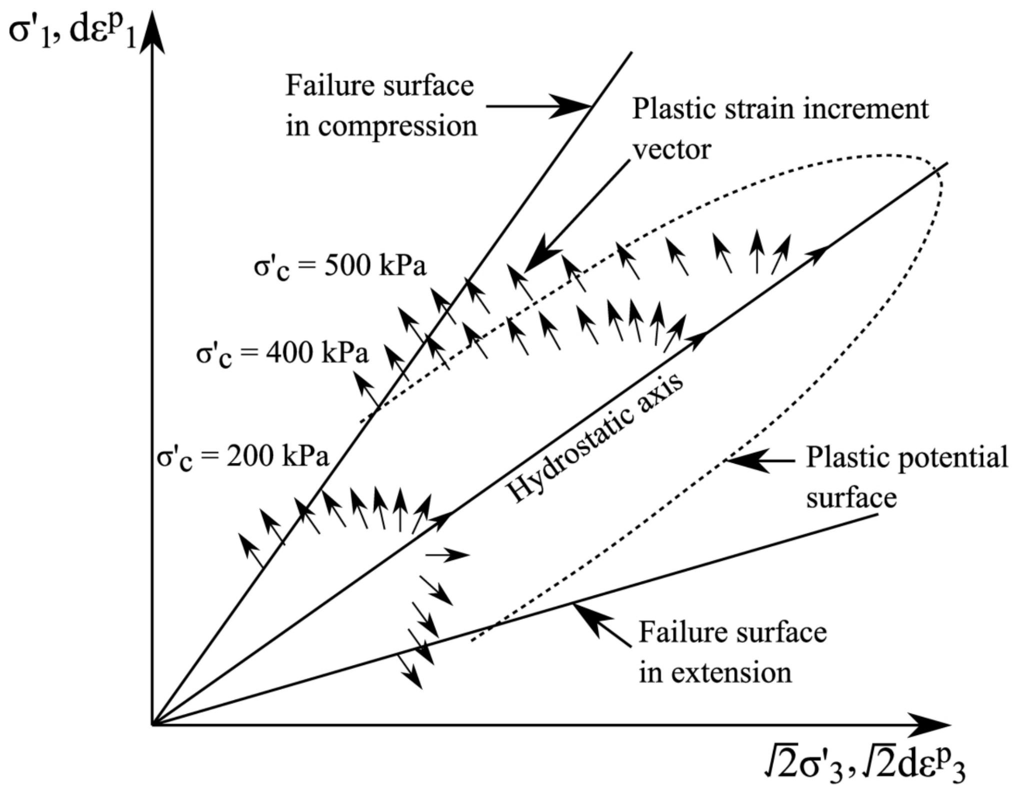

Fig. 15. Directions of plastic strain increment vectors in triaxial plane for triaxial compression tests (b = 0.0) and true triaxial extension (b = 1.0) test on Soil 1.

200x155mm (300 x 300 DPI)

© The Author(s) or their Institution(s)